Journal of Alloys and Compounds 521 (2012) 77–82

Contents lists available at SciVerse ScienceDirect

Journal of Alloys and Compounds

journal homepage: www.elsevier.com/locate/jallcom

Photoluminescence properties of $Y_5Si_3O_{12}N:Ce^{3+}$ blue-emitting phosphors for white LED

Fa-Chun Lu[a,*], Shu-Qing Guo[a], Zhi-Ping Yang[a], Yan-Min Yang[a], Pan-Lai Li[a], Xu Li[a], Quan-Lin Liu[b]

[a] College of Physics Science & Technology, Hebei University, Baoding 071002, PR China
[b] State Key Laboratory for Advanced Metals and Materials, School of Materials Science & Engineering, University of Science and Technology Beijing, Beijing 100083, PR China

ARTICLE INFO

Article history:
Received 7 November 2011
Received in revised form 5 January 2012
Accepted 7 January 2012
Available online 16 January 2012

Keywords:
$Y_5Si_3O_{12}N$
Structure
Ce^{3+}
Photoluminescence
Phosphor

ABSTRACT

Blue oxonitridosilicate phosphors with compositions of $(Y_{1-x}Ce_x)_5Si_3O_{12}N$ (x = 0–0.1) have been synthesized. The structures, photoluminescence properties and the relations between the structure and luminescence have been investigated and discussed. The atomic positions and the lattice parameters of $Y_5Si_3O_{12}N$ were acquired. Y atoms occupy two crystallographic sites (Y(1) and Y(2)) in the structure. Ce^{3+} ions were substituted for Y^{3+} ions and two types of photoluminescence centers ($Ce(1)^{3+}$ and $Ce(2)^{3+}$) have been formed. The excitation and emission processes of $Ce(1)^{3+}$ and $Ce(2)^{3+}$ photoluminescence centers were identified and studied. The concentration- and temperature-dependent properties of these $Y_5Si_3O_{12}N:Ce^{3+}$ phosphors were investigated. This study shows these blue $Y_5Si_3O_{12}N:Ce^{3+}$ phosphors the potential applications in the three-RGB phosphor-converted white LEDs.

1. Introduction

Compared with incandescent and fluorescent lamps, InGaN-based white-emitting diodes (WLEDs) show many advantages, such as a long lifetime, a small volume, toxic-free and energy-saving materials [1]. There are three different methods that can be used to realize the white light emitting: red–green–blue (RGB) light emitting diode (LED) chips combined directly; blue-LED chip combined with yellow (or 'green and red') wavelength conversion phosphor, near-ultraviolet LED chip combined with RGB wavelength conversion phosphor. The latter two methods are usually adopted because they are economic and easy for production. In the both methods the conversion phosphors are playing an important role. These phosphors must have the excellent luminescent features that they can be efficiently excited by the blue-LED chip or near-ultraviolet LED chip and emit efficiently in blue, green, yellow, or red wavelengths.

Now large interests have been focused on the Ce^{3+}/Eu^{2+} doped nitridosilicate and oxonitridosilicate due to their potential application as novel phosphors for WLEDs [2,3]. The emission and absorption spectra of the Ce^{3+}/Eu^{2+} ion usually consist of broad bands due to the transitions between the ground state of the $4f^1/4f^7$ configuration and the lower excited states (the crystal field splitting components of the 5d configuration). The emission varies from UV to red, depending on the host lattice because of a strong interaction of the 5d-electron with the neighboring anion ligand in the compounds [4,5].

The structure of nitridosilicate typically consists of SiN_4 tetrahedra. The nitrogen of SiN_4 tetrahedra can be partially replaced by the oxygen to form $Si[O/N]_4$ tetrahedra. SiN_4 or $Si[O/N]_4$ units are stacked together by sharing their corners or edges to form a condensed framework, resulting in the excellent thermal and chemical stability of nitridosilicate and oxonitridosilicate. Rare-earths or other metal ions can be accommodated in the voids of the network. These various structures can provide the Ce^{3+}/Eu^{2+} with rich and different ligand environments, and adjust the emission and absorption wavelengths. Some compounds have been extensively studied, such as Ca-α-SiAlON:Eu^{2+} [6], β-SiAlON:Ce^{3+} [7], $SrSi_2O_2N_2:Eu^{2+}$ [8], $Ba_3Si_6O_{12}N_2:Eu^{2+}$ [9], $CaAlSiN_3:Eu^{2+}$ [10], $M_1M_2Si_4N_7:Eu^{2+}$ (M_1 = Ca, Sr, Ba; M_2 = Al, Y) [11,12] and $BaSi_3Al_3O_4N_5:Eu^{2+}$ [13]. The above luminescent materials combined the unique luminescence characteristics from 5d to 4f transitions of rare-earth ions and the thermal and chemical stability of host materials.

In Y–Si–O–N quaternary system there are five crystalline phases that have been identified and studied: $Y_2Si_3O_3N_4$, $Y_4Si_2O_7N_2$, $Y_5Si_3O_{12}N$, $YSiO_2N$, and $Y_3Si_5N_9O$ [14,15]. These compounds are always needing critical synthesis conditions, such as high temperature and high pressure. Moreover, the structures of the Y–Si–O–N compounds have not been completely identified and studied; while limited interest has been paid to the photoluminescence (PL) properties. Besides our work [16,17], only a few papers have reported the PL properties of the rare-earths doped Y–Si–O–N compounds [18–20]. In the paper of van Krevel [18], the authors have reported

* Corresponding author. Tel.: +86 312 5079354; fax: +86 312 5079354.
E-mail address: LuFaChun@hbu.edu.cn (F.-C. Lu).

0925-8388/$ – see front matter © 2012 Elsevier B.V. All rights reserved.
doi:10.1016/j.jallcom.2012.01.044

the excitation and emission spectra of the $Y_5Si_3O_{12}N:Ce^{3+}$ phosphor. And they discussed the relations between the PL properties and the number ratios of N^{3-} to O^{2-} ions in the structure of the Y–Si–O–N compounds. But the crystal structure, the concentration-dependent properties, the temperature-dependent properties and the relations between the structure and the luminescence have not been reported yet.

In this work, we synthesized a series of Ce^{3+} doped $(Y_{1-x}Ce_x)_5Si_3O_{12}N$ (x = 0–0.10) phosphors by a novel synthetic route based on a solid state reaction among YSi, CeSi, SiO_2 and Y_2O_3 at high temperature and high nitrogen pressure. We refined the crystal structure of $Y_5Si_3O_{12}N$ and studied the PL properties of the $Y_5Si_3O_{12}N:Ce^{3+}$ phosphors. The relations between the structure and the PL property were investigated.

2. Experimental

2.1. Synthesis of $Y_5Si_3O_{12}N:Ce^{3+}$

The starting materials are metallic Y, Ce and Si powder and high purity Y_2O_3 powder (>99.99%). YSi and CeSi alloys were firstly prepared by argon arc melting of an appropriate amount of the starting materials. To ensure the homogeneity of the alloys the ingots were turned and melted several times. The raw materials, i.e. YSi, CeSi, and Y_2O_3, were weighed according to the desired compositions, and then mixed, ground and pressed into pellets. Thereafter polycrystalline $(Y_{1-x}Ce_x)_5Si_3O_{12}N$ (x = 0, 0.001, 0.005, 0.01, 0.02, 0.03, 0.04, 0.06, 0.08 and 0.1) samples were prepared by a solid state reaction. The pellets were sintered at about 1873 K for 3 h under high-purity nitrogen atmosphere (>99.999%) in a graphite furnace. The starting nitrogen atmosphere pressure is 0.3 MPa. The samples were cooled down with the furnace. These samples were ground and sintered three times in order to reach equilibrium.

2.2. Characterization of $Y_5Si_3O_{12}N:Ce^{3+}$

The X-ray diffraction (XRD) data for lattice parameter refinements were collected on a Philips X'Pert PW-3040 diffractometer (45 kV × 40 mA) with Cu $K\alpha_1$ radiation (λ = 0.15406 nm). Continuous scan mode with a 2θ range of 10°–80° was employed. The XRD data for atomic position refinements were collected on a Rigaku D/max 2500 diffractometer (50 kV × 250 mA) with Cu Kα radiation and a graphite monochromator. Step scan mode was employed with a step width of 2θ = 0.02° and a sampling time of 1 s. The 2θ scan range is 10°–120°. These XRD data were analyzed by the Rietveld refinement program FullProf.2k (Version 2.40). A pseudo-Voigt function was used for the profile function.

The PL spectra at room temperature were recorded on a Hitachi F-4500 Fluorescence Spectrophotometer with a 200 W Xe-lamp as an excitation source. The spectrum resolution is 1.0 nm and the wavelength accuracy is ±2.0 nm. Spectrum correction has been performed in order to measure the true spectrum by eliminating the instrumental response such as wavelength characteristics of the monochromator or detector using Rhodamine B as an internal standard. Bandpass for both excitation and emission monochromators were kept at 5.0 nm. The wavelength scan speed was 1200 nm min^{-1} and Photo Multiplier Tube (PMT) voltage was fixed at 400 V. The wavelength scan range is 250–700 nm. The PL spectra on the low temperature were measured with an Edinburgh Instruments FLS920 Spectrofluorimeter equipped with a continuous Xe-lamp (450 W). The sample was mounted on a closed cycle cryostat (10–350 K, DE202, Advanced Research Systems). Slit widths of 0.3 nm each were used on the excitation and emission monochromators. The step width is 1.0 nm and the dwell time is 0.20 s. The line intensities and positions of the measured spectra were calibrated using the FLS920 correction curve and a standard mercury lamp.

3. Results and discussion

3.1. X-ray powder diffractions and structure

The powder XRD patterns of samples $(Y_{1-x}Ce_x)_5Si_3O_{12}N$ (x = 0, 0.04 and 0.1) in the region of 20°–60° are shown in Fig. 1. These XRD patterns match well with the reported pure $Y_5Si_3O_{12}N$ XRD pattern (JCPDS No. 48-1625). In some samples there is existing small amount of $Y_4Si_2O_7N_2$ (JCPDS No. 86-1106) as impurity phase. With increasing Ce concentration, the XRD pattern shifts slightly to lower angles. Hence the lattice parameters expand when more Ce content is added to the material. In this experiment, the lattice parameters of the each sample were acquired by the Rietveld refinements. The initial model structure used for $Y_5Si_3O_{12}N$ lattice parameter and atomic position refinements is $La_5Si_3O_{12}N$, which was reported in the paper of Titeux et al. [21]. The $Y_4Si_2O_7N_2$ atomic positions and lattice parameters used for these refinements were adopted with our experimental results, which were reported in our previous paper [16].

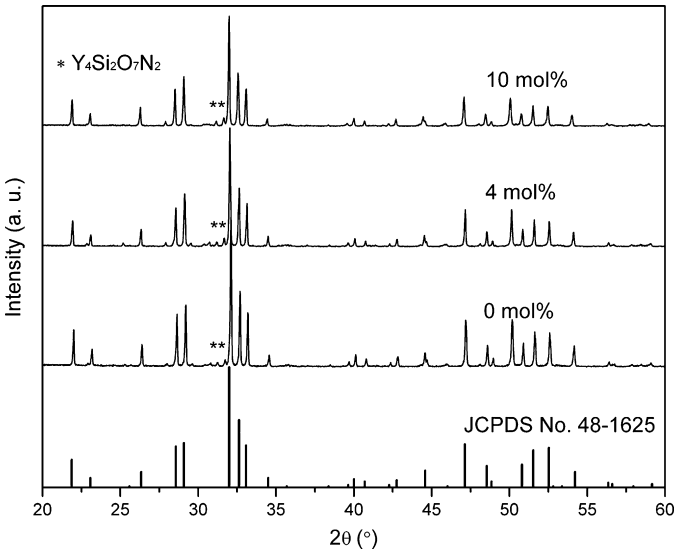

Fig. 1. Powder XRD patterns of the synthesized $(Y_{1-x}Ce_x)_5Si_3O_{12}N$ (x = 0, 0.04 and 0.1) samples.

Rietveld refinement technique is a whole-pattern-fitting method of refining crystal structures from powder diffraction data. By adjusting the atomic and profile shape parameters, least-squares fitting is used to fit the calculated profile shape with the observed [22,23]. In most of the Rietveld refinement programs in use, at least with X-ray data, lattice parameters are refined simultaneously with the others and surprisingly precise lattice parameters are obtained as a benefit incidental to the main purpose [24]. In this experiment, the refined lattice parameters a (b), c and cell volume V of the $(Y_{1-x}Ce_x)_5Si_3O_{12}N$ (x = 0–0.1) samples are shown in Table 1. The vary relations of the lattice parameters with the Ce concentration are shown in Fig. 2. The lattice parameters a (b), c and cell volume V are expanding linearly with increasing Ce concentration. These vary relations are in agreement with the Vegard's law [25–27] with the radius of Ce^{3+} (1.03 Å) larger than that of Y^{3+} (0.90 Å). The linear-increasing relations indicate that the Ce^{3+} ions have been doped in the lattice and substituted for the Y^{3+} ions.

Similar to the model structure of $La_5Si_3O_{12}N$, $Y_5Si_3O_{12}N$ belongs to the hexagonal system and the space group is $P63/m$ (No. 176). Its structure has two formula units in a unit cell, i.e. a unit cell contains 10Y + 6Si + 24O + 2N atoms. The Y, Si, O and N atoms correspondingly occupy 6h + 4f, 6h, 2a + 6h + 6h + 12i and 12i Wyckoff positions in the structure, respectively. Fig. 3 shows the Rietveld refinement results of $Y_5Si_3O_{12}N$. In the figure, the middle vertical bars

Table 1
Refined lattice parameters a (b), c and cell volume V of $(Y_{1-x}Ce_x)_5Si_3O_{12}N$ (x = 0–0.1).

x	a (b) (Å)	c (Å)	V (Å^3)
0	9.3542 (1)	6.7634 (1)	512.518 (3)
0.001	9.3543 (1)	6.7635 (1)	512.528 (3)
0.005	9.3543 (1)	6.7640 (1)	512.571 (3)
0.01	9.3554 (1)	6.7654 (1)	512.800 (3)
0.02	9.3586 (1)	6.7680 (1)	513.345 (3)
0.03	9.3644 (1)	6.7721 (1)	514.297 (3)
0.04	9.3678 (1)	6.7747 (1)	514.873 (3)
0.06	9.3736 (1)	6.7791 (1)	515.846 (3)
0.08	9.3827 (1)	6.7867 (1)	517.424 (3)
0.1	9.3909 (1)	6.7922 (1)	518.749 (3)

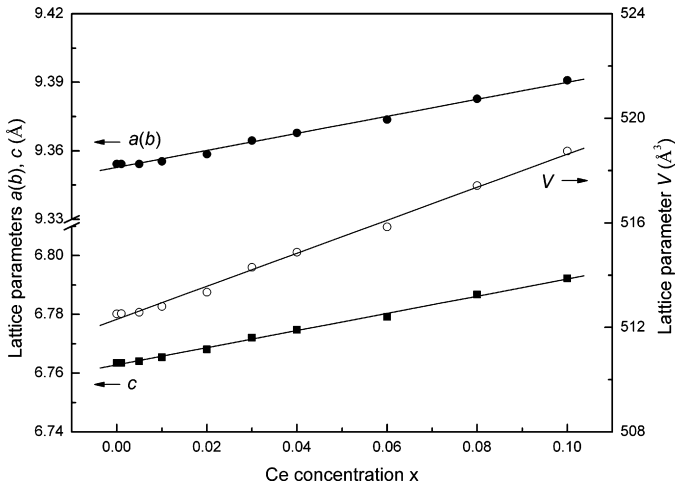

Fig. 2. Variations of the lattice parameters a (b), c and cell volume V of $(Y_{1-x}Ce_x)_5Si_3O_{12}N$ (x = 0–0.1) with the increasing Ce concentration x.

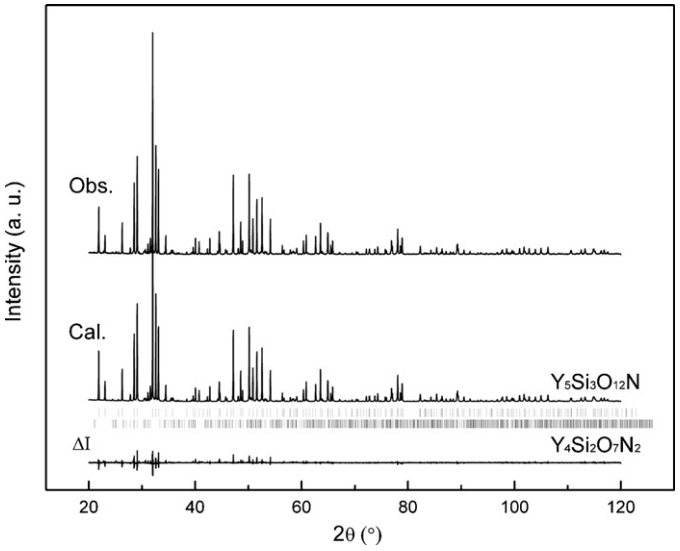

Fig. 3. Observed and calculated X-ray patterns of $Y_5Si_3O_{12}N$. The lowest curve shows the difference between them. From up to down the vertical bars show the expected Bragg reflection positions of $Y_5Si_3O_{12}N$ and $Y_4Si_2O_7N_2$.

from up to down indicate the expected Bragg reflection positions of $Y_5Si_3O_{12}N$ and $Y_4Si_2O_7N_2$. The lowest curve is the difference between the observed and calculated XRD patterns. The reliability factors of this Rietveld refinement are R_p = 10.30%, R_{wp} = 14.00% and R_{exp} = 7.77%, respectively. Table 2 shows the refined equivalent sites and atomic coordinates of $Y_5Si_3O_{12}N$. The center projection structure of $Y_5Si_3O_{12}N$ is shown in Fig. 4(a). In the structure Y atoms occupy two types of crystallographic sites (Wyckoff positions 6h and 4f). The ratio of the number of Y atoms in the two sites is 3:2. Y(1) atoms are coordinated by 7 O/N atoms with an average inter-atomic distance of 2.51 Å. Y(2) atoms are coordinated by 9 O/N atoms with an average inter-atomic distance of 2.62 Å. The coordinated atoms and the bond lengths of the two Y occupied sites are listed in Table 3. Fig. 4(b) shows the coordinated O/N atoms of Y(1) and Y(2) sites.

Table 2
Equivalent sites and refined atomic coordinates of $Y_5Si_3O_{12}N$.

Atom	Wyckoff position	*X*	*Y*	*Z*	S.O.F.
Y(1)	6h	0.2339 (1)	−0.0021 (1)	0.2500	1.0
Y(2)	4f	0.3333	0.6667	0.0006	1.0
Si	6h	0.3999 (1)	0.3751 (1)	0.2500	1.0
O(1)	2a	0.0000	0.0000	0.2500	1.0
O(2)	6h	0.3175 (2)	0.4898 (2)	0.2500	1.0
O(3)	6h	0.6002 (2)	0.4720 (2)	0.2500	1.0
O(4)	12i	0.3417 (2)	0.2531 (1)	0.0612 (2)	0.8333
N	12i	0.3417 (2)	0.2531 (1)	0.0612 (2)	0.1667

Table 3
Inter-atomic distances between Y and coordinated O/N atoms.

Y	O/N	*d* (Å)	Y	O/N	*d* (Å)
	O(1)	2.2809	Y(2)	O(2)	2.4437
	O(3)	2.4777		O(2)	2.4438
	O(4)/N	2.4399		O(2)	2.4438
	O(4)/N	2.4399		O(3)	2.5223
Y(1)	O(4)/N	2.5496		O(3)	2.5223
	O(4)/N	2.5496		O(3)	2.5223
	O(2)	2.8116		O(4)/N	2.8801
				O(4)/N	2.8801
				O(4)/N	2.8801
Mean		2.507			2.616

3.2. Photoluminescence properties

With the increase of the monitor wavelengths (λ_{mon}), the excitation spectra vary regularly. Fig. 5 shows the measured excitation spectra of the 4 mol% Ce doped sample under the λ_{mon} of 400, 425, 452, 475, 500 and 550 nm. The excitation spectra show a broad excitation band corresponding to the transition from the Ce^{3+} $4f^1$ ground state ($^2F_{5/2}$) to the lowest 5d splitting level. Two excitation peaks (P1 and P2) are observed in the excitation band, which are attributed to the absorption of the different PL centers in the lattice. In $Y_5Si_3O_{12}N$ Y^{3+} ions occupy two crystallographic sites. When

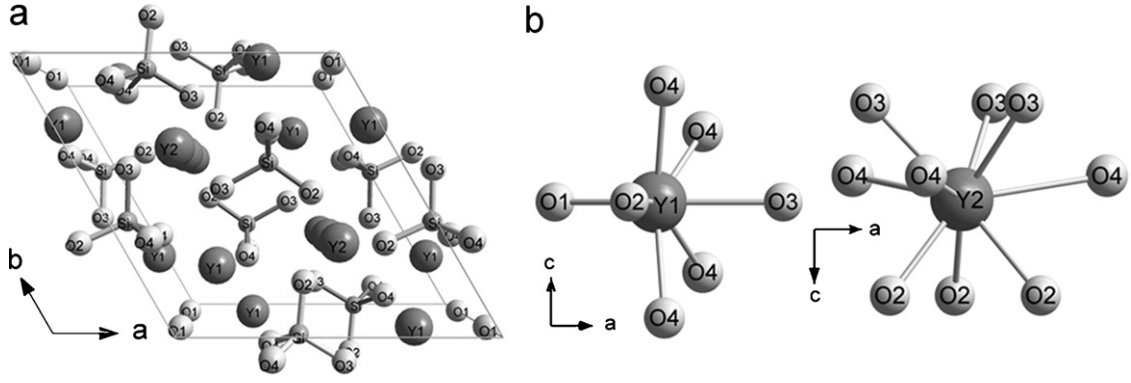

Fig. 4. (a): Center projection structure of $Y_5Si_3O_{12}N$; (b): Coordinated O/N atoms of Y(1) and Y(2) central cations.

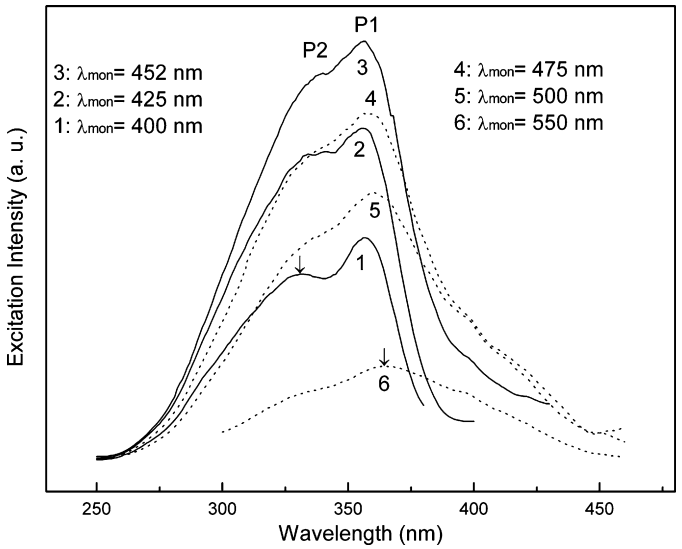

Fig. 5. The excitation spectra of the 4 mol% Ce doped sample under λ_{mon} of 400, 425, 452, 475, 500 and 550 nm.

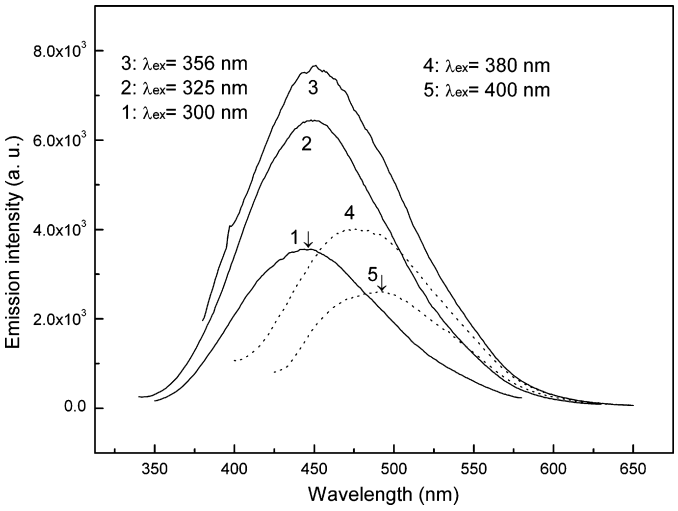

Fig. 6. The emission spectra of the 4 mol% Ce doped sample under λ_{ex} of 300, 325, 356, 380 and 400 nm.

Ce^{3+} ions are substituted for Y^{3+} ions in the lattice, the Ce^{3+} ions generate two types of PL centers because of the different ligands' environments. For Ce^{3+} ions, the energy state of the exposed 5d electron is intensively disturbed by the crystal field and splitting to several energy levels with a maximum number of 5. As reported by Dorenbos [28], the crystal splitting intensity of the Ce^{3+} 5d electron is inversely proportion to the inter-atomic distance between the central cation and the coordinated atoms. In the crystal structure of $Y_5Si_3O_{12}N$, Y(1) site has a smaller average inter-atomic distance than Y(2) site. Hence the crystal splitting intensity of the $Ce(1)^{3+}$ 5d electron is larger than that of the $Ce(2)^{3+}$ 5d electron. The two excitation peaks (P1 and P2) are, respectively, ascribed to the absorption of the $Ce(1)^{3+}$ and $Ce(2)^{3+}$ PL center. The excitation spectra in this figure are the overlapped excitation spectra of the two types of PL centers. When λ_{mon} is located at 452 nm (Spectrum 3 in Fig. 5), the PL intensity of the excitation spectrum reaches the maximum. We selected this spectrum as the main excitation spectrum of this sample. In Fig. 5, the two wavelength positions (364 and 331 nm) of the two signed excitation peaks (signed with '↓') were selected as the excitation wavelengths of $Ce(1)^{3+}$ and $Ce(2)^{3+}$ PL centers of this sample.

Similar to the excitation spectra, the emission spectra of this phosphor also show regular variations when changing the excitation wavelengths (λ_{ex}). Fig. 6 shows the measured emission spectra of the 4 mol% Ce doped sample under the λ_{ex} of 300, 325, 356, 380 and 400 nm. These emission spectra are the overlapped emissions of the two types of PL centers. At λ_{ex} of 356 nm (Spectrum 3 in Fig. 6), the emission spectrum has much higher intensity than the others. We selected this spectrum as the main emission spectrum of this sample. With the increase of the λ_{ex}, the emission peak shifts from 445 to 491 nm. The wavelength positions (491 and 445 nm) of the two signed emission peaks (signed with '↓' in Fig. 6) were selected as the emission wavelengths of $Ce(1)^{3+}$ and $Ce(2)^{3+}$ PL centers of

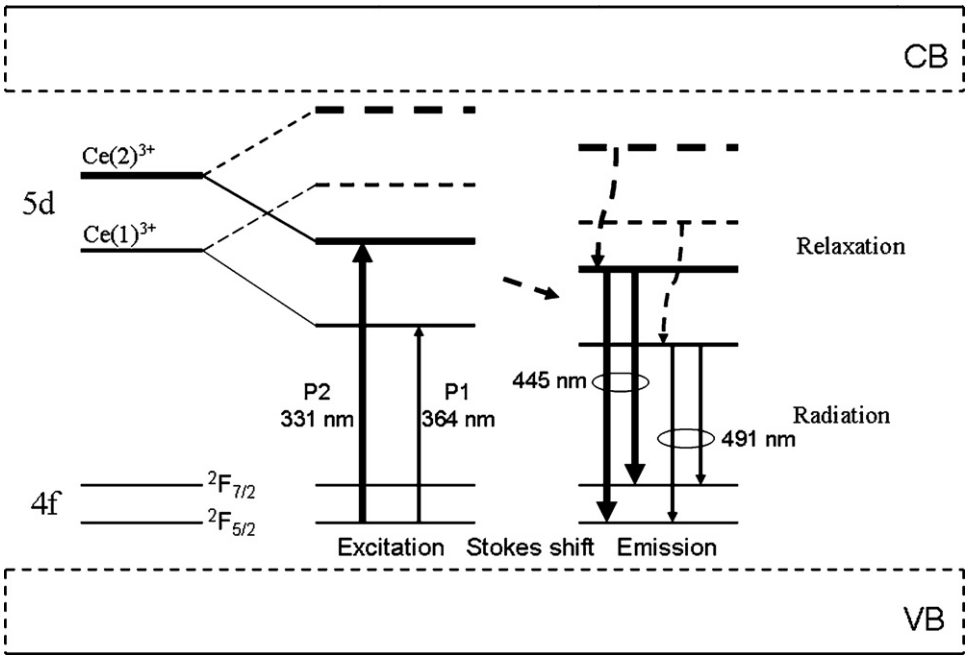

Fig. 7. An schematic energy diagram of the 5d electron of the $Ce(1)^{3+}$ and $Ce(2)^{3+}$ PL centers in the forbidden band of the 4 mol% Ce doped sample.

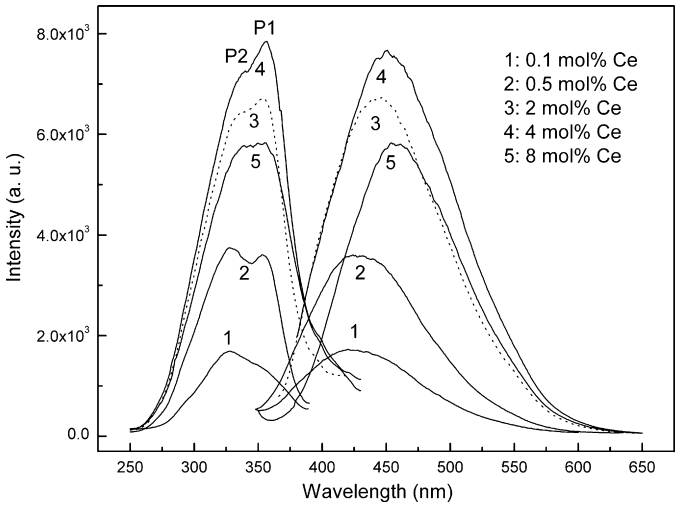

Fig. 8. The main excitation and emission spectra of the Ce^{3+} doped $(Y_{1-x}Ce_x)_5Si_3O_{12}N$ ($x = 0.001$, 0.005, 0.02, 0.04, 0.08) samples. Spectra 1: $\lambda_{ex} = 326$ nm, $\lambda_{mon} = 420$ nm; 2: $\lambda_{ex} = 330$ nm, $\lambda_{mon} = 425$ nm; 3: $\lambda_{ex} = 354$ nm, $\lambda_{mon} = 442$ nm; 4: $\lambda_{ex} = 356$ nm, $\lambda_{mon} = 450$ nm; 5: $\lambda_{ex} = 355$ nm, $\lambda_{mon} = 457$ nm.

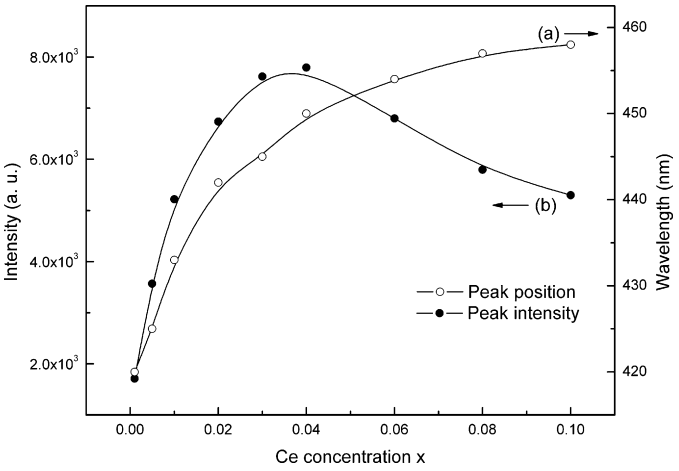

Fig. 9. (a): Red shift of the emission spectra from Ce concentration 0.1 mol% to 10 mol%. (b): Variation of the emission intensity with the increasing Ce concentrations.

this sample. Then the stokes shifts of the $Ce(1)^{3+}$ and $Ce(2)^{3+}$ PL centers in this phosphor are ~7106 and 7739 cm^{-1}, respectively.

Under the analyses of the crystal structure and the PL spectra, an schematic energy diagram of the 5d electron of the $Ce(1)^{3+}$ and $Ce(2)^{3+}$ PL centers in the forbidden band of the 4 mol% Ce doped sample can be given, which is shown in Fig. 7.

Fig. 8 shows the main excitation and emission spectra of the Ce^{3+} doped $(Y_{1-x}Ce_x)_5Si_3O_{12}N$ samples with $x = 0.001$, 0.005, 0.02, 0.04 and 0.08. The emission spectra of these phosphors cover much broad wavelength bands of 350–650 nm. For lower Ce concentration samples, in the excitation spectra the PL intensity of P2 is higher than that of P1 (Spectrum 1 and 2 in Fig. 8). For higher Ce concentration samples the PL intensity of P1 becomes stronger than that of P2 (Spectrum 3, 4 and 5 in Fig. 8). The reason for this phenomenon is that the doped Ce atoms are preferably to occupy the bigger Y polyhedron for the lower Ce concentration samples. As discussed above, the O/N polyhedron size of Y(2) is bigger than that of Y(1). So for the lower Ce concentration samples P2 has a higher PL intensity than P1. When more Ce atoms are doped in the host, the doped Ce atoms tend to be distributed equally over the sites of Y(1) and Y(2). In the crystal structure of $Y_5Si_3O_{12}N$ the number ratio of Y(1) to Y(2) is 3:2. So for the higher Ce concentration samples the PL intensity of P1 is higher than that of P2.

With the increase of Ce concentrations, the emission spectrum shifts to longer wavelength band, i.e. red shift. From the Ce concentration 0.1 mol% to 10 mol%, the emission peak red-shifts from 420 to 458 nm, as shown in Fig. 9(a). Several mechanisms can be used to explain the red shift. One of the mechanisms is that the more Ce atoms doped in the lattice leads to an increase of the crystal field splitting [29–32]. The increasing crystal field splitting lowers the lowest 5d splitting energy and the excitation and emission energy is lowered. One of the proofs for the increase of the crystal field splitting is the red shift of the excitation peaks. But as shown in Fig. 8, the P1 and P2 excitation peaks only show slight red shifts with the increase of Ce concentrations. So this mechanism of the increase of the crystal field splitting may be not the main mechanism leading to the emission red shift of this phosphor. In Fig. 8, we can see that the stokes shift increases when more Ce atoms are doped in the host. And there are some overlapped band between the excitation and the emission spectra. So the other mechanisms, stokes shift and radiation re-absorption, may be the possible mechanisms for the emission red shift of this phosphor. And maybe the several mechanisms mentioned above are co-operating in this phosphor.

With increasing Ce concentration, concentration quenching occurs. Concentration quenching usually occurs as a result of the non-radiative energy transfer among the luminescence centers. Two mechanisms are usually adopted to explain the non-radiative energy transfer, i.e., multipolar interaction and radiation re-absorption. In the mechanism of multipolar interaction, the probability of energy transfer between the two activator ions is inversely proportional to the nth power of R' ($n = 6$, 8, or 10) where R' is the distance between the activator ions [33,34]. With the increasing Ce content doped in the lattice, the inter-atomic distance between the two activators becomes smaller, and then the probability of energy transfer becomes higher. Thereafter the PL intensity is quenched for the higher Ce concentration samples. And because of the overlapped band between the excitation and emission spectra, the radiation re-absorption effect may also play an important role for the concentration quenching. On one hand, the radiation re-absorption lowers the emission intensity for the higher Ce concentration sample. On the other hand, the radiation re-absorption reduces the intensity of the high-energy wing of the Ce^{3+} emission band, leading to the red shift of the emission spectra. The variation of the emission intensity dependent on Ce concentration is shown in Fig. 9(b). The emission intensity reaches the maximum when Ce concentration is 4 mol%.

The PL spectra of the 0.1 mol% Ce doped sample in the temperature ranges of 10–300 K have been measured. In Fig. 10, the insert figures show the excitation and emission spectra of this phosphor at temperatures of 10, 100, 250 and 300 K. From 10 to 300 K, the excitation and emission spectra show similar spectrum profiles. With the increase of the temperature, the spectral intensity quenches, i.e. thermal quenching. In Fig. 10, the main figure shows the variation of the PL intensity of the emission spectra dependent on the temperature. Several mechanisms can be used to explain the thermal quenching of the phosphors. A widely accepted mechanism is the electronic transition through the intersection between the ground and excited states, in other words this mechanism is described as a large displacement between the ground and excited state in the configuration coordinate diagram [35]. Other quenching mechanisms, for example thermal excitation of 5d electrons to conduction band sates [36] or excitation of holes from Ce to the valence band states [37], were also suggested [38]. And for most of the Ce^{3+}/Eu^{2+} doped phosphors, the thermal quenching variations can be fitted and explained with the Boltzmann model [38,39]. But in this experiment, in the temperature range of 50–200 K, the thermal

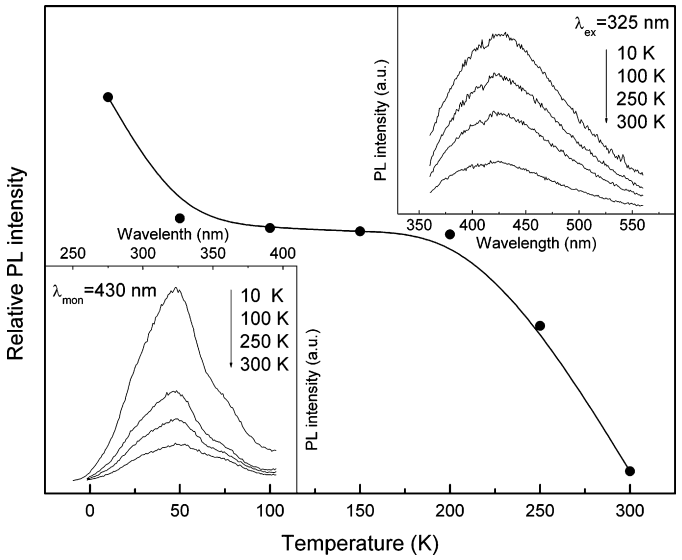

Fig. 10. Main figure: Variation of the emission intensity of the 0.1 mol% Ce doped sample with increasing temperature. Insert figures: Excitation and emission spectra at temperatures of 10, 100, 250 and 300 K.

quenching shows a flat variation. And in the temperature ranges of 10–50 K and 200–300 K, the PL intensity quenches more quickly. Up to our knowledge now, we cannot confirm the reason which leads to this variation. With increasing temperature, the excitation and emission spectra nearly show no shift. The Stokes shift of this phosphor is stable against the temperature. The reason may be that this material has the rigid structure frameworks of $Si[O/N]_4$ tetrahedral. Hence the chromaticity coordinates of the excitation and emission spectra of this phosphor are stable against the temperature. This property can be in favor of keeping the chromaticity and brightness of the white light output of the WLEDs.

4. Conclusions

We have synthesized oxonitridosilicate phosphors with compositions of $(Y_{1-x}Ce_x)_5Si_3O_{12}N$ (x = 0–0.1) by the solid-state reaction, and reported their structures and luminescent properties. Y atoms occupy two crystallographic sites in $Y_5Si_3O_{12}N$ structure. Y(1) site has a smaller average inter-atomic distance than Y(2) site. The splitting intensity of the 5d electron of $Ce(1)^{3+}$ ions is stronger than that of $Ce(2)^{3+}$. Two types of Ce^{3+} PL centers formed. These phosphors show the overlapped excitation and emission spectra of the $Ce(1)^{3+}$ and $Ce(2)^{3+}$ PL center. When the doped Ce concentration is 4 mol%, the PL intensity of this $Y_5Si_3O_{12}N:Ce^{3+}$ phosphor reaches the maximum. With the increase of the Ce concentration, the emission spectra show red shift. The chromaticity coordinates of the excitation and emission spectra of this phosphor are stable against the temperature. These phosphors have the potential applications in the three-RGB phosphor-converted WLEDs.

Acknowledgements

This work is supported by National Natural Science Foundation of China (No. 90922027) and the National High Technology Research and Development Program of China (No. 2009AA03Z432).

References

[1] S. Ye, F. Xiao, Y.X. Pan, Y.Y. Ma, Q.Y. Zhang, Mater. Sci. Eng. Rep. 71 (2010) 1–34.
[2] R.-J. Xie, N. Hirosaki, Y.Q. Li, T. Takeda, Materials 3 (2010) 3777–3793.
[3] H. Yamamoto, Proc. SPIE 7598 (2010) 759808.
[4] P. Dorenbos, J. Lumin. 91 (2000) 155–176.
[5] P. Dorenbos, J. Lumin. 104 (2003) 239–260.
[6] W.J. Park, Y.H. Song, J.W. Moon, S.M. Kang, D.H. Yoon, Solid State Sci. 12 (2010) 1853–1856.
[7] J.H. Ryu, H.S. Won, Y.-G. Park, S.H. Kim, W.Y. Song, H. Suzuki, C.-B. Yoon, D.H. Kim, W.J. Park, C. Yoon, Electrochem. Solid State Lett. 13 (2010) H30–H32.
[8] Y.H. Song, W.J. Park, D.H. Yoon, J. Phys. Chem. Solids 71 (2010) 473–475.
[9] J.Y. Tang, J.H. Chen, L.Y. Hao, X. Xu, W.J. Xie, Q.X. Li, J. Lumin. 131 (2011) 1101–1106.
[10] B.F. Lei, K. Machida, T. Horikawa, H. Hanzawa, Chem. Lett. 39 (2010) 104–105.
[11] T. Kurushima, G. Gundiah, Y. Shimomura, M. Mikami, N. Kijima, A.K. Cheetham, J. Electrochem. Soc. 157 (2010) J64–J68.
[12] J. Ruan, R.-J. Xie, N. Hirosaki, T. Takeda, J. Am. Ceram. Soc. 94 (2011) 536–542.
[13] J.-Y. Tang, W.-J. Xie, K. Huang, L.-Y. Hao, X. Xu, R.-J. Xie, Electrochem. Solid State Lett. 14 (2011) J45–J47.
[14] W.Y. Ching, L.Z. Quyang, H.Z. Yao, Y.N. Xu, Phys. Rev. B 72 (2004) 085105.
[15] Y.N. Xu, P. Rulis, W.Y. Ching, Phys. Rev. B 72 (2005) 113101.
[16] F.C. Lu, X.P. Song, Q.L. Liu, Opt. Mater. 33 (2010) 91–98.
[17] F.C. Lu, X.Y. Chen, M.W. Wang, Q.L. Liu, J. Lumin. 131 (2011) 336–341.
[18] J.W.H. van Krevel, H.T. Hintzen, R. Metselaar, A. Meijerink, J. Alloys Compd. 268 (1998) 272–277.
[19] H.C. Yang, Y. Liu, S. Ye, J.R. Qiu, Chem. Phys. Lett. 451 (2008) 218–221.
[20] D.G. Deng, S.Q. Xu, X.Y. Su, Q. Wang, Y.Q. Li, G.F. Li, Y.J. Hua, L.H. Huang, S.L. Zhao, H.P. Wang, C.X. Li, Mater. Lett. 65 (2011) 1176–1178.
[21] S. Titeux, M. Gervais, P. Verdier, Y. Laurent, Mater. Sci. Forum 325–326 (2000) 17–20.
[22] H.M. Rietveld, Acta Crystallogr. 22 (1967) 151–152.
[23] H.M. Rietveld, J. Appl. Crystallogr. 2 (1969) 65–67.
[24] R.A. Young, D.B. Wiles, J. Appl. Crystallogr. 15 (1982) 430–438.
[25] L. Vegard, Z. Phys. 5 (1921) 17–26.
[26] L. Vegard, Z. Kristallogr. 67 (1928) 239.
[27] A.R. Denton, N.W. Ashcroft, Phys. Rev. A 43 (1991) 3161–3164.
[28] P. Dorenbos, J. Alloys Compd. 341 (2002) 156–159.
[29] H.A. Hoppe, H. Lutz, P. Morys, W. Schnick, A. Seilmeier, J. Phys. Chem. Solids 61 (2000) 2001–2006.
[30] J.W.H. van Krevel, J.W.T. van Rutten, H. Mandal, H.T. Hintzen, R. Metselaar, J. Solid State Chem. 165 (2002) 19–24.
[31] R.-J. Xie, N. Hirosaki, M. Mitomo, Y. Yamamoto, T. Suehiro, J. Phys. Chem. B 108 (2004) 12027–12031.
[32] R.-J. Xie, N. Hirosaki, T. Suehiro, F.F. Xu, M. Mitomo, Chem. Mater. 18 (2006) 5578–5583.
[33] B. Dierre, R.-J. Xie, N. Hirosaki, T. Sekiguchi, J. Mater. Res. 22 (2007) 1933–1941.
[34] J.R. Qiu, K. Miura, N. Sugimoto, K. Hirao, J. Non-Cryst. Solids 213–214 (1997) 266–270.
[35] G.H. Munoz, C.L. de la Cruz, A.F. Munoz, J.O. Rubio, J. Mater. Sci. Lett. 7 (1988) 1310–1312.
[36] U. Happek, S.A. Basun, J. Choi, J.K. Krebs, M. Raukas, J. Alloys Compd. 303–304 (2000) 198–206.
[37] H. Najafov, A. Kato, H. Toyota, K. Iwai, A. Bayramov, S. Iida, Jpn. J. Appl. Phys. 41 (2002) 2058–2065.
[38] P. Dorenbos, J. Phys.: Condens. Matter 17 (2005) 8103–8111.
[39] R.-J. Xie, N. Hirosaki, N. Kimura, K. Sakuma, M. Mitomo, Appl. Phys. Lett. 90 (2007) 191101.